Investigation of magnetic coupling in FePt/spacer/FePt trilayers

A Kaidatzis[1], G Giannopoulos[1], G Varvaro[2], G Dimitrakopulos[3], V Psycharis[1], J M Garcia-Martin[4], A M Testa[2], G Barucca[5], T Karakostas[3], P Komninou[3] and D Niarchos[1]

[1] Institute of Nanoscience and Nanotechnology, NCSR Demokritos, Athens, Greece
[2]ISM-CNR, Area della Ricerca RM1, P.B. 10-00015, Monterotondo Scalo, Roma, Italy
[3]Department of Physics, Aristotle University of Thessaloniki, GR-54124 Thessaloniki, Greece
[4] IMN-Instituto de Micro y Nanotecnología (CNM-CSIC), Isaac Newton 8, PTM, E-28760, Tres Cantos, Madrid, Spain
[5]Università Politecnica delle Marche, Dipartimento SIMAU, Via Brecce Bianche, Ancona 60131, Italy

E-mail: a.kaidatzis@inn.demokritos.gr

Abstract. The effect of different spacer materials (MgO, W, and Pt) on the magnetic coupling in FePt/spacer/FePt trilayers has been carefully investigated. MgO results in magnetically coupled FePt layers with perpendicular magnetic anisotropy (PMA); W gives rise to a magnetically coupled system consisting of layers with PMA and in-plane magnetic anisotropy whereas Pt results in magnetically decoupled FePt layers with PMA. The trilayer microstructure is essential for explaining the obtained results. The growth mode of the top FePt layer is strongly affected by the underlying non-magnetic spacer, with occurrence of different morphologies; in particular, $L1_0$ FePt islands grow on MgO, a continuous FePt layer with fcc crystal structure is obtained on W, whereas a continuous layer with $L1_0$ structure is observed when the top layer is deposited on Pt.

Keywords. 3D magnetic recording; $L1_0$ FePt; magnetic coupling; XRD; magnetometry; TEM; MFM

1. Introduction

There is a constant demand for increasing data storage capacity of hard disk drives, beyond the limit of 1 Tbit/in^2 recording areal density of state-of-the-art technologies (1). A promising route for achieving this goal is 3-dimensional (3D) magnetic recording, where magnetically decoupled ferromagnetic layers with different magnetic properties are vertically stacked and separated by a non-magnetic spacer. By so doing multi-level data storage may be implemented (2; 3), thus allowing increasing data storage density while maintaining adequately large magnetic bits for long-term storage. In the past, a 4-level magnetic signal has been experimentally demonstrated in Co/Pd-spacer-Co/Pd magnetic trilayer dot arrays (4), while recently an 8-level signal has been demonstrated in Co/Pt-spacer-Co/Pd-spacer-Co/Pd multilayers (5). Layer-selective writing and readout methods were proposed for realizing this technology (6; 7) and recently experimentally demonstrated in CoFeB-spacer-CoPt trilayers (8; 9).

In this work we have studied the magnetic properties of FePt/spacer/FePt trilayers for exploring their potential as 3D magnetic recording media. The chemically ordered fct FePt phase (usually dubbed $L1_0$) with perpendicular magnetic anisotropy (PMA) is currently considered the best candidate for next generation magnetic recording media due to its high uniaxial magnetic anisotropy ($K_u \approx 5\times$

10^7erg/cm^3), which allows smaller thermally stable grains, ultimately down to 4 nm (10; 11; 12; 13). One of the mandatory requirements for implementing 3D magnetic recording is to obtain magnetically decoupled ferromagnetic layers for independently controlling the magnetisation of each layer. Moreover, the magnetic coupling in FePt/spacer/FePt trilayers with PMA is of interest for other applications, such as pseudo-spin-valves and magnetic tunnel junctions and it has been already studied using MgO (14), Pt and Pd (15), Ag (16), and TiN (17) as spacer materials. In these works the magnetic coupling was found to depend on spacer thickness and type (insulating vs. metallic), magnetic layer, as well as on its magnetic microstructure. In the present work, three spacer materials have been studied – W, MgO, and Pt – yielding trilayers with different magnetic behaviour, which is explained in terms of the crystallographic structure and microstructure of the stacks.

2. Experimental details

Sample deposition has been performed in an ultra-high vacuum (base pressure 1.5×10^{-9} Torr) magnetron sputtering system (AJA ATC-2200-V) in diode configuration. FePt(20 nm)/spacer(5 nm)/FePt(10 nm) trilayer stacks have been deposited on commercial monocrystalline (001) MgO substrates with low surface roughness (~ 0.1 nm), which would favour the formation of the $L1_0$ FePt phase with a (001) texture (i.e. *c*-axis, corresponding to the magnetic easy-axis, perpendicular to the film plane) (18). Homogeneous deposition was ensured by rotating the substrates around their normal axis. The source material was a round 50 mm diameter $Fe_{50}Pt_{50}$ target. High purity Ar (99.999%) was used as sputtering gas at 3 mTorr pressure. The applied DC power was 2 W/cm^2, yielding a deposition rate of 0.041 nm/s. The substrates were kept at 500°C during deposition for promoting the formation of the magnetically hard $L1_0$ fct phase with alternate stacking of (0 0 1) planes of Fe and Pt instead of the softer fcc phase (labelled A1) (19). The spacers were also deposited at 500°C, using pure metallic W or Pt targets, or a stoichiometric MgO target; RF power was used in the latter case. In order to support the investigation of trilayers, single FePt films with a nominal thickness of 10 and 20 nm were also deposited using the same experimental conditions.

X-ray diffraction (XRD) structural analysis has been performed using a Siemens D500 diffractometer with Cu-K_α radiation, in steps of 0.03° and counting time 6 s/step. θ-2θ scans were obtained in the 18° to 120° range. Transmission Electron Microscopy (TEM) analyses have been carried out by a Philips CM200 microscope operating at 200 kV and equipped with a LaB_6 filament. High resolution TEM (HRTEM) observations have been performed using a 200 kV JEOL 2011 microscope (point resolution 0.19 nm, Cs = 0.4 mm). For TEM observations, samples have been prepared by mechanical grinding, comprising dimpling and/or tripod polishing. Final thinning was carried out by ion milling in a Gatan PIPS using 5 kV Ar^+ ions. Superconducting quantum interference device (SQUID) magnetometry has been performed using a Quantum Design MPMS instrument, equipped with a superconducting 50 kOe magnet.

Magnetic Force Microscopy (MFM) has been performed using a Bruker Dimension Icon microscope and commercial probes from Bruker (MESP-HM). Probes were magnetized along their axis, which is perpendicular to the sample surface; thus, the obtained magnetic contrast originated from the magnetic poles at the surface, which can be ascribed to magnetic domains with perpendicular magnetization. The samples were demagnetized using an alternating out-of-plane field with decreasing amplitude prior imaging. MFM images were obtained using the phase imaging double-pass tapping-mode: surface topography was recorded during the first pass and then the tip was lifted at a certain height above the sample and the phase shift induced by the magnetic interaction between tip and sample was recorded. All microscopy images have been processed using the WSxM software (20).

3. Results and discussion

3.1 Single FePt films

Figure 1a shows XRD θ-2θ graphs of single 10 and 20 nm thick FePt layers. In both cases, the fundamental (002) and (004) and the superlattice (001) and (003) Bragg peaks of the $L1_0$ FePt structure can be clearly detected. The strong Bragg peaks produced by the MgO (001) substrate are

also apparent. The chemical ordering parameter *S* of the films is calculated by taking into account the integrated intensities of the (001) and (002) peaks; pseudo-Voigt fits to the data are employed (21). High chemical ordering is obtained in both the samples, as the *S* parameter is 0.72±0.06 and 0.71±0.06 at the 10 and 20 nm thick films, respectively. The calculated lattice constant is c=0.37±0.02 nm and the $d_{(002)}$ spacing is 0.187±0.009 nm, in both cases.

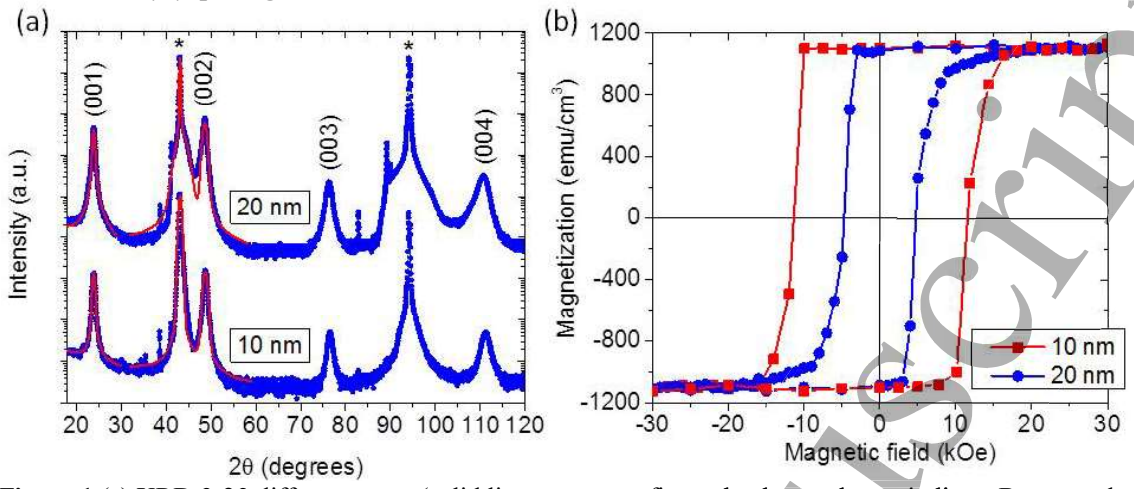

Figure 1 (a) XRD θ-2θ diffractograms (solid lines represent fits to the data and stars indicate Bragg peaks of the MgO substrate) and (b) room temperature hysteresis cycles (the magnetic field was applied perpendicularly to the sample surface) of the 10 and 20 nm single FePt films.

Figure 1b shows room temperature SQUID magnetometry hysteresis cycles of the single FePt layers, obtained with the magnetic field applied perpendicularly to the samples' surface. A saturation magnetization value of 1100±15 emu/cm^3, was measured for both the films, being it very close to the bulk $L1_0$ FePt value (22). The coercive field (H_C) greatly decreases from 11.0 kOe at the 10 nm thick film to 4.7 kOe at the 20 nm thick film. The larger H_C of the thinner film is attributed to its non-continuous microstructure (23; 24; 25) (see figure 2).

Figure 2 shows cross-section TEM images of single nominally 10 and 20 nm thick FePt layers grown on (001) MgO substrates. Strikingly different growth morphology is observed in the two cases. The nominally 20 nm thick film is continuous, with a real thickness equal to 22±1 nm. In the case of the nominally 10 nm thick film, the film morphology is discontinuous with partially coalesced elongated islands with average real thickness equal to 14±2 nm. . This behaviour shows a 3D growth mode whereby the initially formed islands extend laterally with increasing thickness, and finally coalesce into a continuous film. In the continuous film, introduction of inclined twins and stacking faults on {111} planes (see arrows on the image) appears to be promoted by the interfacial roughness in addition to the 8.5% misfit with the substrate.

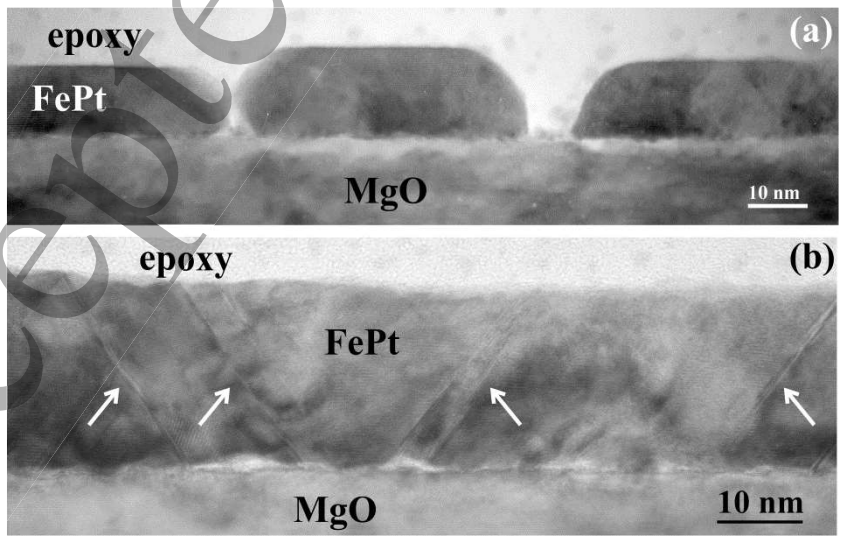

Figure 2 HRTEM images of the 10 nm thick (a) and 20 nm thick (b) single FePt layers.

Figure 3 shows high magnification cross-sectional HRTEM images of selected grains in each sample, along with their corresponding diffractograms obtained by fast Fourier transform (FFT). The image of the 10 nm thick film was obtained along the [100]MgO//[100]FePt direction, whereas the image of the 20 nm thick film was obtained along the [110] zone axis. In both cases, highly textured (001) FePt films with a $L1_0$ crystal structure form, although, in the case of the 20 nm thick film, the presence of twins introduce some local deviations of the growth axis from the [001] direction. The MgO/FePt interface roughness is higher in the case of the thicker film, indicating a more severe intermixing; this could be attributed to the longer time spent at 500°C by the interface during the deposition of the 20 nm thick FePt layer. The FFT diffractograms show superlattice reflections due to $L1_0$ FePt ordering.

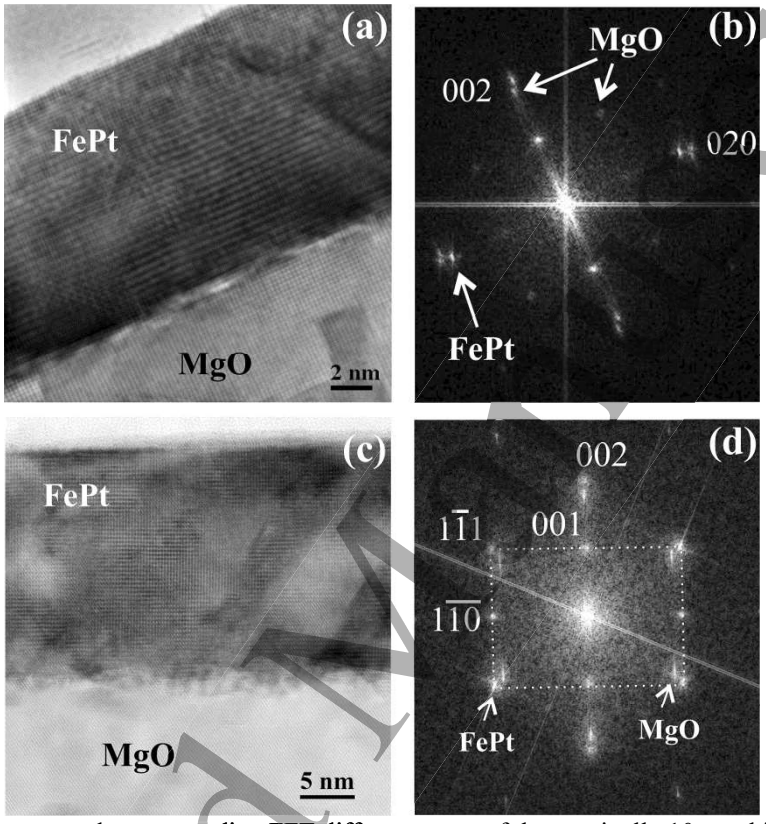

Figure 3 HRTEM images and corresponding FFT diffractograms of the nominally 10 nm thick (a, b) and 20 nm thick (c, d) FePt single layers.

3.2 FePt/spacer/FePt trilayers

Due to its continuous nature, the magnetic trilayers have been fabricated using a 20 nm thick bottom FePt layer. On top, a non-magnetic spacer was deposited, followed by a 10 nm thick top FePt layer, whose thickness is such that a different H_C with respect to the bottom layer is expected.

TEM analysis has been performed to investigate the morphology and structure of the trilayers. Figure 4a shows a typical TEM bright-field image of the trilayer having a 5 nm thick MgO spacer. Both the bottom FePt layer and the MgO spacer grow forming a continuous and uniform film. The two layers have thicknesses in agreement with the nominal values and their interface roughness is low. The FePt top layer, on the other hand, exhibits an island growth. The morphology and size of the islands are completely similar to those observed in the single 10 nm thick FePt layer deposited directly on the MgO substrate. In Figure 4b the corresponding SAED pattern is reported. Diffraction spots of the $L1_0$ ordered FePt phase in the <100> zone axis orientation are identified (dashed cell). Furthermore, diffraction spots of the MgO in the <100> zone axis are also clearly visible (dotted cell). Considering that other diffraction spots are not present and that the large arrow in Figure 4b indicates the direction perpendicular to the substrate, the following growth orientations for the different layers can be deduced: MgO substrate ‖ {001}$L1_0$ ‖ {001}MgO ‖‖ {001}$L1_0$. In particular, SAED measurements indicate the same orientation and structure for the two FePt layers as well as for the

MgO spacer and substrate. To confirm these last results, dark field imaging was also performed. A typical dark field image obtained selecting the (021) $L1_0$ diffraction spot of Figure 4b is shown in Figure 4c. In the image, the crystalline areas of the sample responsible of that particular diffraction spot appear brighter, thus revealing that both the FePt layers have the same $L1_0$ structure and crystallographic orientation. The dark field image of Figure 4d is obtained selecting the (0-2-2) MgO reflection of Figure 4b. The MgO spacer and substrate appear brighter in the figure confirming the same crystallographic orientation and structure.

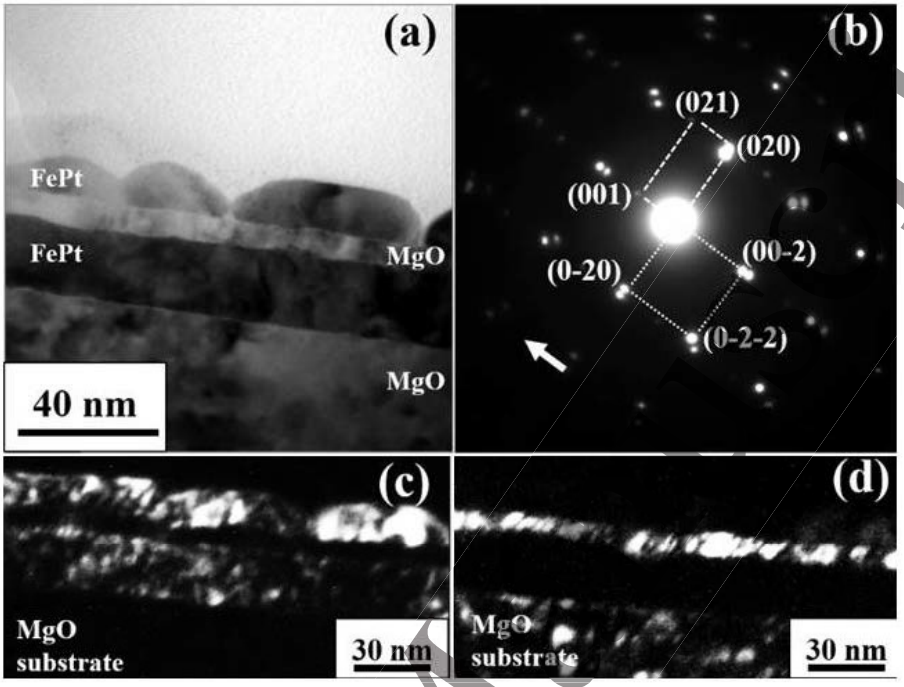

Figure 4 TEM analysis of the FePt/MgO/FePt trilayer. (a) Bright-field image. (b) Corresponding SAED pattern: rectangular dashed cell corresponds to the $L1_0$ phase in [100] orientation; squared dotted cell corresponds to the MgO phase in [100] orientation; the large arrow indicates the direction perpendicular to the substrate. Dark-field image obtained selecting: (c) the (021) $L1_0$ reflection; (d) the (0-2-2) MgO reflection.

Striking differences are observed when W is used as the non-magnetic spacer. Figure 5a shows a TEM bright-field image of the FePt(20 nm)/W(5 nm)/FePt(10 nm) trilayer. All three layers grow forming continuous and uniform films with thicknesses in good agreement with the nominal values. The interfaces among the layers are well detectable and show low roughness. The corresponding SAED pattern is shown in Figure 5b. Diffraction spots of the $L1_0$ ordered FePt phase in the <100> zone axis orientation are identified (dashed cell), together with diffraction spots of the cubic A1 disordered FePt phase in the <110> zone axis (dotted cell). Other intense diffraction spots are visible in the image and can be attributed to the W and MgO grains oriented in the <100> zone axis. For sake of clarity, the corresponding cells are not reported in figure 5b and only the (011)W and the (002)MgO diffraction spots are indicated. Considering that in figure 5b, the large arrow indicates the direction perpendicular to the substrate, SAED measurements give the following growth orientations for the different layers: MgO substrate ‖ {001}$L1_0$ ‖ {011}W ‖ {111}A1.

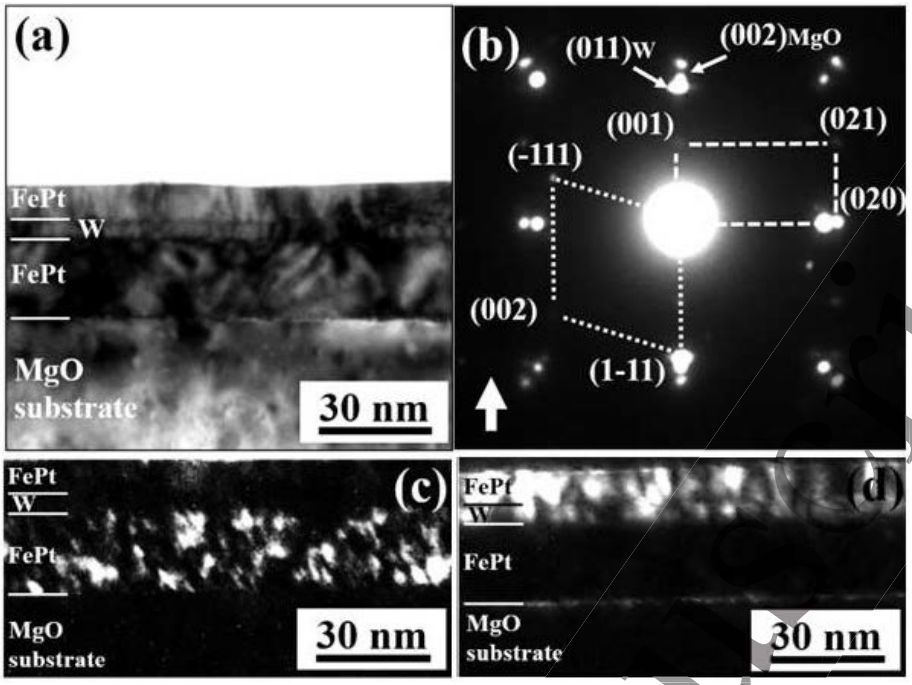

Figure 5 TEM analysis of the FePt/W/FePt trilayer. (a) Bright-field image. (b) Corresponding SAED pattern: rectangular dashed cell corresponds to the $L1_0$ phase in [100] orientation; rhombohedral dotted cell corresponds to the A1 phase in [110] orientation; the large arrow indicates the direction perpendicular to the substrate. Dark-field image obtained selecting: (c) the (001) $L1_0$ reflection; (d) the (1-11) A1 reflection.

To spatially identify the position of the two FePt phases, dark field images were performed using the corresponding reflections. Figure 5c, obtained selecting the $L1_0$ (001) reflection of Figure 5b, shows that the FePt layer in contact with the MgO substrate has the ordered $L1_0$ structure. Selecting the A1 (1-11) reflection, the image of Figure 5d is obtained. The top FePt layer has the A1 structure. In this case, even the W layer appears lighter in the image. This effect is related to the objective aperture used to select the (1-11)A1 diffraction spot. The finite dimension of the aperture does not prevent that other diffracted signals go through the aperture. In particular, very close to the (1-11)A1 diffraction spot, the reflection coming from the {011}W lattice planes is present and also the W layer appears bright.

TEM analysis of the FePt(20 nm)/Pt(5 nm)/FePt(10 nm) trilayer is summarized in Figure 6. Bright field images do not allow the different layers to be distinguished. Only a single continuous and uniform film is visible in Figure 6a having a thickness of about 36 nm, in good agreement with the sum of the three layers' nominal thicknesses. A typical SAED pattern of the sample is shown in Figure 6b. Diffraction spots of the $L1_0$ ordered FePt phase in the <100> zone axis orientation are identified (rectangular dashed cell), together with diffraction spots of the cubic MgO phase in the <100> zone axis (not indicated in Figure 6b). Reflections coming from the Pt phase are not clearly visible because they are positioned between the MgO and $L1_0$ spots. In particular, the squared dotted cell of Figure 6b shows the position of the diffraction spots coming from the Pt phase in <100> zone axis. SAED measurements indicate the same orientation and structure for the two FePt layers and considering that in Figure 6b the large arrow indicates the direction perpendicular to the substrate, the following growth orientations for the different layers can be deduced: MgO substrate ‖ {001}$L1_0$ ‖ {001}Pt ‖ {001}$L1_0$. In Figure 6c, a dark field image of the trilayer obtained by selecting the $L1_0$ (021) reflection is illustrated. The different layers can be now easily distinguished, confirming the same $L1_0$ crystallographic structure and orientation for the two FePt layers. If the $L1_0$ (002) reflection is selected, the dark field image of Figure 6d is obtained. All the three layers appear brighter in this case because the finite dimension of the objective aperture used to obtain the dark field image cannot prevent the Pt {002} reflection to contribute to the image.

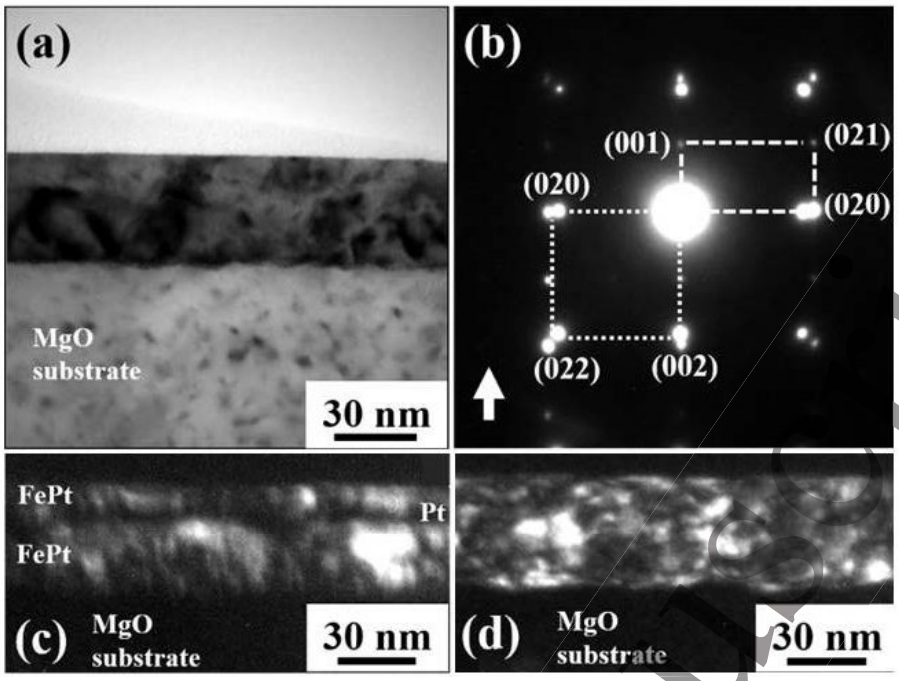

Figure 6 TEM analysis of the FePt/Pt/FePt trilayer. (a) Bright-field image. (b) Corresponding SAED pattern: rectangular dashed cell corresponds to the $L1_0$ phase in [100] orientation; squared dotted cell corresponds to the Pt phase in [100] orientation; the large arrow indicates the direction perpendicular to the substrate. Dark-field image obtained selecting: (c) the (021) $L1_0$ reflection; (d) the (002) $L1_0$ reflection.

Figure 7a shows the demagnetizing branch of hysteresis loops measured at room temperature with the external field applied along the direction perpendicular to film plane. The corresponding field derivative dM/dH curves are shown in figure 7b. A nearly-single magnetisation switching occurs when W and MgO are used as spacers; while a two-step magnetisation switching is clearly observed in the FePt/Pt/FePt sample. Moreover, a decrease of the saturation magnetisation (M_S) of the trilayer samples compared to the single FePt layers is observed. The lowest M_S is found when MgO spacer is used (860 emu/cm^3), whereas larger values are obtained for W and Pt spacers (940 and 970 emu/cm^3, respectively). The decreased M_S of the trilayers may be attributed to interface mixing at the top and bottom FePt/spacer interfaces, which leads to the creation of a magnetic dead layer. It is assumed that the presence of MgO should lead to a strong interface mixing which is expected to be weaker in the case of W and Pt.

The shape of the hysteresis curves also shows differences between the samples. When MgO is used as spacer, the hysteresis curve shows an initial abrupt magnetisation decay followed by a very slow magnetisation reversal. The initial abrupt decrease is observed at a field lower than the coercivity of the corresponding single layers, thus suggesting that the two FePt layers are magnetically coupled. Both the bottom and the top layers have an $L1_0$ structure and exhibit PMA; however their different morphology (continuous vs. discontinuous) would result in a different coercivity, which is expected to be larger for the discontinuous top layer. In previous works, it has been shown that the magnetic coupling between two layers with PMA (11; 24) is greatly affected by the magnetic microstructure of the hardest magnetic layer, as the stray-field emanating from the domain-walls was found to strongly enhance magnetostatic coupling (25). In our samples, the stray fields emanating at the edges of the top FePt islands should be large enough to initiate the reversal of the bottom FePt layer. In such a case, the reversal is expected to occur through the formation of vertically correlated magnetic domains; the initial abrupt magnetisation decay and the following slow magnetisation variation (observed in the field-dependent magnetization curve) should be interpreted as the nucleation and the annihilation of vertically correlated reverse domains (26).

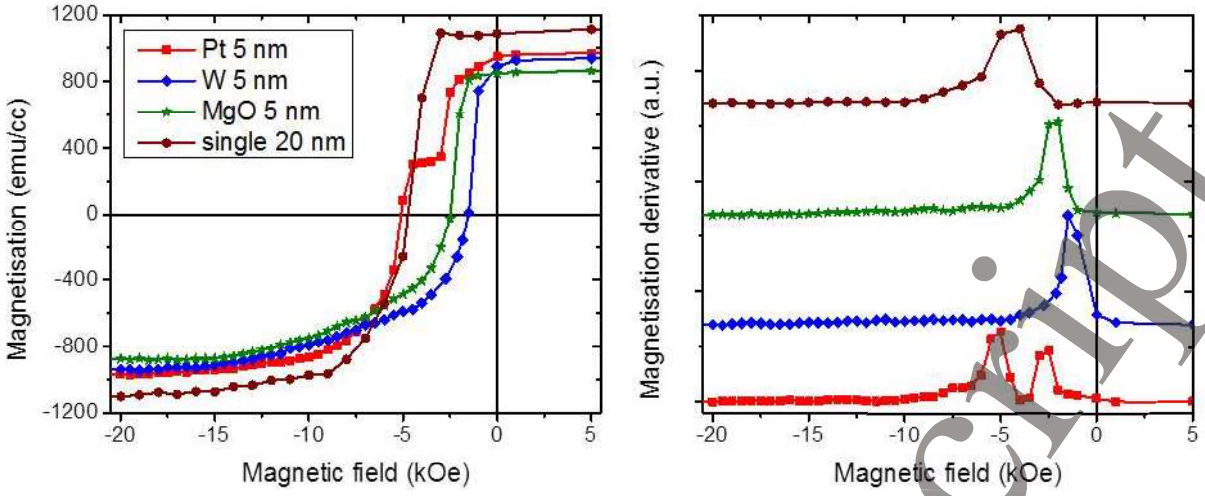

Figure 7 Demagnetizing branch of hysteresis loops (left panel) and its field derivative dM/dH (right panel; the curves are shifted at the vertical axis for clarity purposes) of the FePt(20 nm)/spacer(5 nm)/FePt(10 nm) trilayers and the single 20 nm thick FePt layer. The hysteresis loops were recorded at room temperature with the filed applied perpendicularly to the film plane.

A similar hysteresis curve shape is obtained at the W-spacer trilayer: the two FePt layers appear to be magnetically coupled, although they are both morphologically continuous. RKKY interaction between the two layers can be excluded due to the large thickness of the W spacer layer. Furthermore, TEM analysis shows no presence of structural pinholes in the W spacer that could lead to direct exchange coupling. However, the bottom FePt layer has an $L1_0$ structure and it is magnetically hard with PMA, whereas the top FePt layer has a fcc structure and is magnetically soft with an in-plane anisotropy. The occurrence of such a mixing of magnetic anisotropy of different type (27), results in stray fields (emanating from the bottom layer) large enough to initiate the reversal of the top layer, leading to the observed coupled magnetisation reversal of the two FePt layers via vertically coupled magnetic domains (26; 28; 29).

In the Pt-spacer case, TEM and SAED data show that both layers are continuous and have an $L1_0$ crystal structure with the c-axis oriented perpendicularly to the film surface. From the amplitude of the first jump in the hysteresis loops, it can be deduced that the lowest H_C (2.7 kOe) corresponds to the top layer, since its thickness is half of that of the bottom layer. Moreover, the highest H_C value is 5 kOe, which is comparable to that of the single 20 nm thick layer sample, thus supporting that the second jump at H_c = 5.2 kOe, corresponds to the 20 nm thick bottom layer. It is interesting to note that the H_C value of the top layer is much lower than that of the single 10 nm thick sample due to the different morphology (continuous vs. discontinuous) and its value is also lower than that of the thicker bottom FePt layer, likely because the Pt will lead to a lower amount of defects that behaves as pinning points. Although the coercivity of the top layer is lower than that of the bottom layer, it is sufficiently high to reduce or even suppress the stray-field-induced magnetic coupling and the two layers can reverse their magnetization independently.

Figure 8 shows AFM and MFM images of the trilayers. The morphology obtained using AFM is in qualitative agreement to TEM observations: MgO spacer yields a trilayer surface with higher roughness (1.4 nm), while the grainy morphology is clearly apparent. The trilayer surface is smoother in the two other cases and the roughness is 0.7 nm for W spacer and 0.8 nm for Pt spacer. MFM reveals a demagnetized magnetic structure with magnetic domains several hundred of nm large, much bigger than the average grain size which is a few tens of nm; this indicates a strong magnetic coupling between grains in the films **(30)**. A striking difference is observed between the magnetic structure of the trilayers using MgO or W spacer and the one of the trilayer with Pt spacer: although a two-level contrast (dark/bright) is observed in the former case, a three-level contrast (dark/intermediate/bright) is observed in the latter case. This indicates a magnetically decoupled configuration in the Pt spacer case; as it has been shown in studies of similar magnetic trilayer systems with PMA **(31)**, the apparent intermediate contrast results from partial overlapping of magnetic domains in each layer with anti-parallel magnetization direction. The absence of any intermediate contrast in the case of MgO or W spacer indicates strong magnetic coupling between the two layers and a complete magnetic domain

replication **(32)**, with a non-homogeneous distribution of magnetic domains as suggested by slight prevalence of "dark" or "bright" contrast in figures (d) and (e).

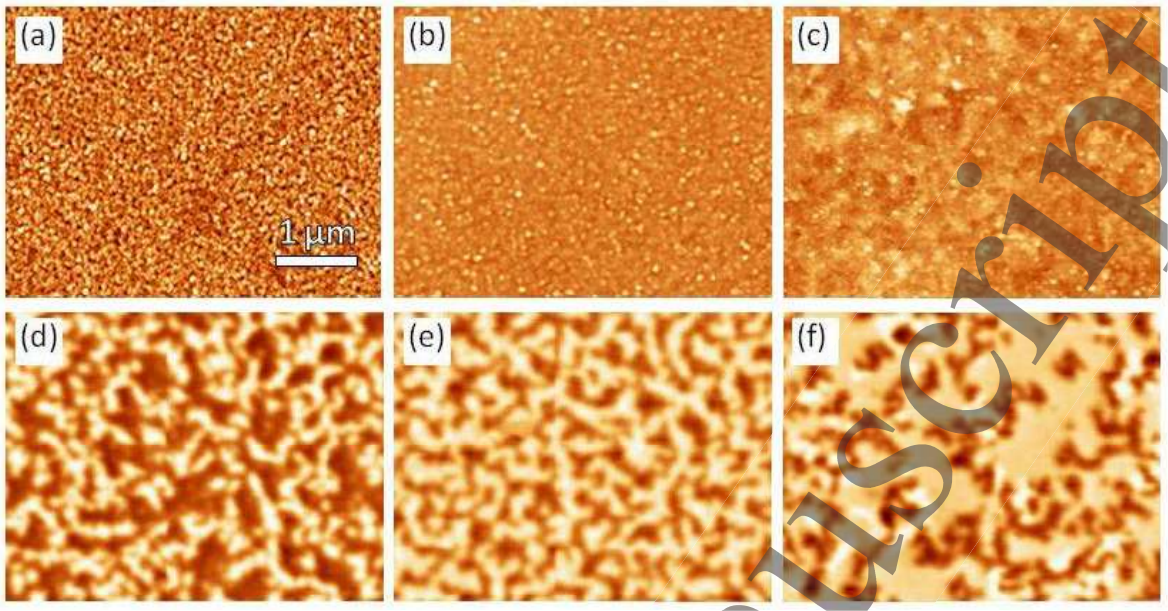

Figure 8 AFM images of the trilayers with (a) MgO spacer, (b) W spacer, and (c) Pt spacer. The vertical scale is 10 nm in all AFM images. Corresponding MFM phase images of the trilayers with (d) MgO spacer, (e) W spacer, and (f) Pt spacer. The vertical scale is 8° in all MFM images. All AFM and MFM images have the same horizontal scale.

4. Summary and conclusions

To summarise, striking differences of the top FePt layer growth mode is observed for each spacer material: $L1_0$ FePt islands develop on MgO, a continuous FePt layer with fcc crystal structure is found for W, whereas a continuous layer with $L1_0$ structure is observed when top layer is deposited on Pt. Subsequently, MgO results in magnetically coupled FePt layers with perpendicular magnetic anisotropy (PMA), W gives rise to a magnetically coupled system consisting of layers with both PMA and in-plane magnetic anisotropy, whereas Pt results in magnetically decoupled FePt layers with PMA. Independent switching of the magnetisation of the two FePt layers is observed only when Pt spacer is used. Taking the above into account, one of the mandatory requirements for 3D magnetic recording media, i.e. an independent control of single layer magnetisation, can be fulfilled by choosing a Pt spacer which yields magnetically decoupled ferromagnetic layers in the final stack.

5. Acknowledgments

Funding from the EC (Grant No. 318144 and 686056) and from CSIC (ref. i-LINK0783), is acknowledged.

6. References

1. *Ultra-High-Density Magnetic Recording: Storage Materials and Media Designs.* **G. Varvaro and F. Casoli,** s.l. : Pan Stanford Publishing, 2016.
2. *J. Magn. Magn. Mater.* **B. Liu and Z.Yuan,** 2001, Vol. 235. 481-486.
3. *Jpn. J. Appl. Phys.* **H. Suto, K. Kudo, T. Nagasawa, T. Kanao, K. Mizushima and R. Sato.** 2016, Vol. 55. 07MA01.
4. *J. Appl. Phys.* **M. Albrecht, G. Hu, A. Moser, O. Hellwig and B. D. Terris.** 2005, Vol. 97. 103910.
5. *PLoS ONE.* **Nissim Amos, John Butler, Beomseop Lee, Meir H. Shachar, Bing Hu, Yuan Tian and Jeongmin Hong.** 2012, PLoS ONE, Vol. 7, p. e40134.

6. *J. Appl. Phys.* . **Shaojing Li, Boris Livshitz, H. Neal Bertram, Eric E. Fullerton and Vitaliy Lomakin.** 2009, Vol. 105. 07B909.
7. *Appl. Phys. Lett.* **G. Winkler, D. Suess, J. Lee, J. Fidler, M. A. Bashir, J. Dean, A. Goncharov,G. Hrkac, S. Bance and T. Schrefl.** 2009, Vol. 94. 232501.
8. *Nanotechnology.* **Hirofumi Suto, Tazumi Nagasawa, Kiwamu Kudo, Koichi Mizushima and Rie Sato.** 2014, Vol. 25. 245501.
9. *Phys. Rev. Appl.* **H. Suto, T. Nagasawa, K. Kudo, T. Kanao, K. Mizushima and R. Sato.** 2016, Vol. 5. 014003.
10. *J. Vac. Sci. Technol. B.* **Dieter Weller, Gregory Parker, Oleksandr Mosendz, Andreas Lyberatos, Dmitriy Mitin, Nataliia Y. Safonova and Manfred Albrecht.** 2016, Vol. 34. 060801.
11. *J. Phys. D: Appl. Phys.* **Tanmay Dutta, Shreya Kundu, M S M Saifullah, Hyunsoo Yang, S N Piramanayagam and C S Bhatia.** 2015, Vol. 48. 445007.
12. *J. Magn. Magn. Mater.* **G. Varvaro, S. Laureti and D. Fiorani.** 2014 йил, Vol. 368. 415–420.
13. *Appl. Surf. Sci.* **Th. Speliotis, G. Varvaro, A.M. Testa, G. Giannopoulos, E. Agostinelli, W. Li, G. Hadjipanayis and D. Niarchos.** 2015, Vol. 337. 118–124.
14. *Phys. Rev. B.* **P. de Person, P. Warin, M. Jamet, C. Beigne and Y. Samson.** 2007, Vol. 76. 184402.
15. *Appl. Phys. Lett.* **A. P. Mihai, J. P. Attané, L. Vila, C. Beigné, J. C. Pillet and A. Marty.** 2009, Vol. 94. 122509.
16. —. **P. Ho, 1,2 G. C. Han, R. F. L. Evans, R. W. Chantrell, G. M. Chow and J. S. Chen.** 2011, Vol. 98. 132501.
17. —. **P. Ho, G. C. Han, K. H. He, G. M. Chow and J. S. Chen.** 2011, Vol. 99. 252503.
18. *J. Appl. Phys.* **J.-U. Thiele, L. Folks, M. F. Toney and D. K. Weller.** 1998, Vol. 84. 5686.
19. *IEEE Trans. Magn.* **D. J. Sellmyer, C. P. Luo, M. L. Yan and Y. Liu.** 2001, Vol. 37. 1286.
20. *Rev. Sci. Instrum.* **I. Horcas, R. Fernández, J. M. Gómez-Rodríguez, J. Colchero, J. Gómez-Herrero and A. M. Baro.** 2007, Vol. 78. 013705.
21. *Phys. Stat. Solidi - Rapid Res. Lett.* **A Kaidatzis, V Psycharis, G Giannopoulos, J M García** -Martín and D Niarchos.
22. *IEEE Trans. Magn.* **D Weller, A Moser, L Folks, M E Best, W Lee, M F Toney, M Schwickert, J-U Thiele and M F. Doerner.** 2000, Vol. 36. 10.
23. *Mater. Trans.* **T Shima, K Takanashi, G Qing Li and Si Ishio.** 2003, Vol. 44. 1508.
24. *J. Appl. Phys.* **J.-U. Thiele, L. Folks, M. F. Toney and D. K. Weller.** 1998, Vol. 84. 5686.
25. *Phys. Rev. B.* **P de Person, P Warin, M Jamet, C Beigne and Y Samson.** 2007, Vol. 76. 184402.
26. —. **S. M. Mohseni, R. K. Dumas, Y. Fang, J. W. Lau, S. R. Sani, J. Persson, and Johan Akerman.** 2011, Vol. 84. 174432.
27. *Sensors and Actuators A.* **P. Matthes and M. Albrecht,** 2015, Vol. 233. 275.
28. *Appl. Phys. Lett.* **J. E. Davies, D. A. Gilbert, S. M. Mohseni, R. K. Dumas, J. Akerman, and K. Liu.** 2013, Vol. 103. 022409.
29. *IEEE Trans. Magn.* **P. Matthes, S. S. P. K. Arekapudi, F. Timmermann, and M. Albrecht.** 2015, Vol. 51. 4400104.
30. *J. Magn. Magn. Mater.* **Y. Sonobe, D. Weller, Y. Ikeda, K. Takano, M.E. Schabes, G. Zeltzer, H. Do, B.K. Yen and M.E. Best.** 2001, Vol. 235. 424.
31. *Phys. Rev. B.* **V. Baltz, A. Marty, B. Rodmacq and B. Dieny.** 2007, Vol. 75. 014406.

32. *Nature Materials.* **O. Hellwig, T. L. Kirk, J. B. Kortright, A. Berger and E. Fullerton.** 2003, Vol. 2. 112.
33. *Phys. Rev. B.* **T. Hauet, C. M. Günther, B. Pfau, M. E. Schabes, J.-U. Thiele, R. L. Rick, P. Fischer, S. Eisebitt and O. Hellwig.** 2008, Vol. 77. 184421.
34. *J. Magn. Magn. Mater.* **H. R. Hilzinger and H. Kronmuller,** 1976, Vol. 2. 11.
35. *Appl. Phys. Lett.* **S. Wiebel, J.-P. Jamet, N. Vernier, A. Mougin, J. Ferré, V. Baltz, B. Rodmacq and B. Dieny.** 2005, Vol. 86. 142502.
36. *J. Appl. Phys.* **S. Khizroev, Y. Hijazi, N. Amos, and R. Chomko.** 2006, Vol. 100. 063907.
37. *J. Magn. Magn. Mater.* **Yuan, Zhimin and Liu, Bo.** 2001, Vol. 235. 481-486.
38. —.**Y.J. Chen et. al.,** 2012, Vol. 324. 264-268.